Optics Communications 533 (2023) 129304

Contents lists available at ScienceDirect

Optics Communications

journal homepage: www.elsevier.com/locate/optcom

Automatic compact-volume design strategy for unobscured reflective optical systems based on conicoid surfaces

Zheng Qu [a,b,c], Xing Zhong [c,d,*], Kun Zhang [e], Yuanhang Wang [a,b,c], Lei Li [a,b,c], Jiang Liu [c], Chaoli Zeng [c,f]

[a] *Changchun Institute of Optics, Fine Mechanics and Physics, Chinese Academy of Sciences, Changchun 130033, China*
[b] *University of Chinese Academy of Sciences, Beijing 100049, China*
[c] *Chang Guang Satellite Technology Co., Ltd, Changchun 130102, China*
[d] *Key Laboratory of Advanced Technology for Aerospace Vehicles of Liaoning Province, Dalian University of Technology, Dalian 116024, China*
[e] *Institute of Optics and Electronics, Chinese Academy of Sciences, Chengdu 610209, China*
[f] *State Key Laboratory of Structural Analysis for Industrial Equipment, Dalian University of Technology, Dalian 116024, China*

ARTICLE INFO

Keywords:
Off-axis
Joint aberration
Small volume
Simulated annealing algorithm

ABSTRACT

Off-axis reflective optical systems are frequently large in volume to avoid obscuration, and their subsequent optimizations are complex and time-consuming, resulting in volume reduction while sacrificing surface shape complexity. Therefore, this paper proposes an automatic small-volume high-resolution reflective optical system design strategy based on joint aberration model and a global simulated annealing algorithm (SA). The method establishes a comprehensive joint aberration-based imaging quality and volume-constrained evaluation function. Under the premise of ensuring the imaging quality, the volume reduction of two off-axis three-mirror reflective optical systems with large fields of view (FOVs) has been achieved greatly: (1) the volume of the systems with off-axis FOVs was compressed to 22.7% of the conventional method; (2) the volume of the systems with a small F-number, decenter and tilt was compressed to 28.3% of the conventional method, successfully achieving the volume compression of the off-axis reflective optical systems, proving the feasibility and simplicity of this method. This method is more scalable, starting with a conical surface, which can well realize the transition from simple to complex surfaces, providing the choice and comparison of surface types and contributing to the rapid estimation of the system volume.

1. Introduction

Off-axis reflective optical imaging systems offer advantages such as no chromatic aberration, no obscuration, wide working spectrum range, fewer elements, high transmission, good thermal stability, etc. [1–4]. Thus, off-axis reflective optical systems are employed in various fields, such as astronomical telescopes, optical remote sensing [5–8], microscopy [9], lithography [10], spectrometer [11], etc. With the advancement of optical design, imaging optics has evolved from simple coaxial systems to off-axis systems with a large FOV. Meanwhile, the growing application scenes complicate the off-axis reflective optical design. At the same time, the emergence of freeform brings up new possibilities and challenges for developing optical imaging systems [12].

Generally, off-axis reflective systems are designed from a coaxial or a good initial configuration. Especially a good initial configuration is crucial, which determines the ease of subsequent optimization [13,14]. However, off-axis reflective optical systems tend to have larger volumes and worse imaging performance than coaxial systems. Therefore, the application of freeform surfaces to the design of off-axis reflective optical systems not only corrects the asymmetric aberrations existing in off-axis systems and improves the optical system's imaging quality, but also greatly reduces the system volume [15–17]. Freeform mirrors provide more freedom in the optical design process. Still, based on traditional optical design software's damped least square (DLS) method, it is simple to be trapped in a local minimum and fail to obtain an optimal optical system. Therefore, a simple and feasible global optimization design method has become a hot research topic. The global optimization algorithms such as the simulated annealing algorithm (SA) [18], double seed curve extension (SCE) algorithm [19], genetic algorithm (GA) [20,21], particle swarm algorithm (PSA) [22], and deep learning method [23,24], which avoid the problem of poor

---

* Corresponding author.
E-mail address: ciomper@163.com (X. Zhong).

https://doi.org/10.1016/j.optcom.2023.129304
Received 12 December 2022; Received in revised form 5 January 2023; Accepted 24 January 2023
Available online 28 January 2023

optimization due to the failure to jump out of the local optimum, also improve the design efficiency of reflective optical systems. The global SA is employed in this paper to calculate the parameters of off-axis initial points.

Various methods to design freeform optical systems are divided into two branches: direct and indirect design. The first direct design method is generally based on the imaging and construction requirements of the system, and the initial configuration for subsequent optimization is obtained by numerically solving the freeform surface point by point and fitting the freeform surface to be solved. Typical methods for such direct designs include the partial differential equations (PDEs) method [25,26], simultaneous multiple surface (SMS) method [27], point-to-point construction-iteration (CI) method [28,29], etc. Another indirect approach is generally to design off-axis optical systems by starting from a coaxial or a similar system in a patent library and progressively off-axis in the FOVs or by decentering and tilt. Besides, it is also an idea to use the off-axis unobstructed system composed of spherical or quadratic surfaces as the initial configuration for subsequent optimization. Still, at this time, many higher-order aberrations are challenging to be optimized in the later process because of the off-axis design. It is an excellent solution to guide the designer to achieve initial unobstructed configurations with less aberration by using the aberration theory [30,31]. However, few starting-point design methods for off-axis reflective systems address automatic system volume compression. Although system volume can be reduced by employing traditional design methods that include volume constraints, this is a trial-and-error process that requires the participation of designers and usually takes a long time for the design. In this paper, we propose a design method to automatically reduce the volume of off-axis reflective optical systems globally by a joint design evaluation function with good imaging performance.

This paper investigates a starting point design method for automatic volume compression based on joint aberration solution model and volume-constraint evaluation. The contributions can be summarized as follows: Firstly, the off-axis nodal aberration theory (NAT) is derived from the off-axis pupil and off-axis aberration field based on the coaxial NAT. Secondly, the off-axis NAT is scalarized by combining the primary Seidel aberration coefficients. Third, the composite evaluation function under the volume constraints is established, and the thickness gradually decreases as the automatic variable. The SA algorithm searches the global solution for the initial points with a small volume. Finally, the effectiveness and feasibility of this method are demonstrated by two types of off-axis three-mirror reflective unobscured optical design examples with large FOVs. The innovative highlights of this paper are as follows: (1) The method considerably improves the efficiency and accuracy of the design by establishing a more comprehensive evaluation function and adopting a global optimization algorithm; (2) The design process of complex reflective optical systems reduces human intervention and weakens the reliance on experience for traditional optical design; (3) The design method is based on the joint aberration solution model, and the volume can be well controlled throughout the optimization process; (4) The method is more scalable from Conic surfaces and combined with traditional optical design software, it can gradually realize the systematic design of complex surfaces. The surface complexity is effectively reduced while keeping the image quality unchanged, and the system volume is successfully minimized to facilitate the engineering of the design.

2. Design method based on joint aberration evaluation

In this paper, a theoretical model of joint aberration is investigated. At the same time, the constraints of structural parameters are integrated into a complex evaluation function to research the optimal initial configuration of an optical system in the global solution domain. The SA algorithm finally obtains a series of feasible solutions to facilitate the selection of optical systems with different requirements. For optical designers, the evaluation of optical designs should be comprehensive, which requires consideration of system volume, the complexity of the design process, the difficulty of manufacturing optical surfaces, imaging quality, etc. Therefore, based on this model, the structural parameters of the optical system are adopted as independent variables, and iterative calculations are performed at reasonable intervals to finally realize the initial point design of a small-volume reflective optical system. The optimization starts from the initial conicoid surface, and good imaging quality will be obtained by adding the more complex surface. This section is divided into two parts: Section 2.1 establishes the joint aberration solution model, and Section 2.2 introduces the design strategy for compact-volume systems.

2.1. Joint aberration solution model

In general, rotationally symmetric nodal aberrations are well adapted for designing simple coaxial optical systems and analyzing aberrations [32,33]. Nevertheless, for off-axis reflective optical systems with more complex parameter requirements, the theory of rotational symmetry has a significant deviation, making it hard to analyze higher-order aberrations due to off-axis quantities. Notably, the expression of aberrations is more complicated when the pupil is off-axis or when the element is tilted or decentered. To use the complete NAT theoretical model, the model derivation is subsequently performed for the off-axis problem.

Thompson et al. [34] proposed the introduction of the central field off-axis vector $\vec{\delta}_j$ of the aberration field in the rotationally symmetric nodal aberration theory, offering the possibility of aberration evaluation of optical systems with tilted and decentered optical elements. The effective aberration field vector (illustrated in Fig. 1) can be expressed as $\vec{H}_{Aj} = \vec{H} - \vec{\delta}_j$, and thus the non-rotationally symmetric vector aberration theory with aberration field deviations can be obtained as

$$\begin{cases} W_j(\vec{H},\vec{\rho}) = \sum\limits_j W_{040j}(\vec{\rho}\cdot\vec{\rho})^2 + \sum\limits_j W_{131j}\left[(\vec{H}-\vec{\delta}_j)\cdot\vec{\rho}\right](\vec{\rho}\cdot\vec{\rho})\cdots \\ \cdots + \frac{1}{2}\sum\limits_j W_{222j}(\vec{H}-\vec{\delta}_j)^2\cdot\vec{\rho}^2 + \sum\limits_j W_{220mj} \\ \quad \times\left[(\vec{H}-\vec{\delta}_j)\cdot(\vec{H}-\vec{\delta}_j)\right](\vec{\rho}\cdot\vec{\rho})\cdots \\ \cdots + \sum\limits_j W_{311j}\left[(\vec{H}-\vec{\delta}_j)\cdot(\vec{H}-\vec{\delta}_j)\right]\left[(\vec{H}-\vec{\delta}_j)\cdot\vec{\rho}\right] \\ W_{220mj} = W_{220j} + \frac{1}{2}W_{222j} \end{cases} \tag{1}$$

where j regards the order of surfaces in the optical system, W_{040j}, W_{131j}, W_{222j}, W_{220mj}, and W_{311j} are the primary wave aberration coefficients of jth surface.

Meanwhile, for various types of off-axis systems, the FOV off-axis and the pupil off-axis at the entrance pupil, in addition to the deviation of the aberration field, impact the overall system aberration. This paper performs a complete analysis and modeling of the effects of aberrations generated by off-axis quantities for aspheric systems, as shown in Fig. 1. To obtain the impact of the pupil off-axis parameters, introducing the aperture scaling factor M, the pupil center offset vector $\vec{P}_1$ as

$$M = \frac{R_2}{R_1}, \quad \vec{P} = \frac{\vec{P}_1}{R_1}, \quad \vec{\rho} = M\vec{\rho}_1 + \vec{P} \tag{2}$$

where R_1 and R_2 are the aperture radius of before and after pupil off-axis respectively; $\vec{P}$ is the normalized pupil off-axis vector; $\vec{\rho}$ is coaxial normalized aperture vector modified to distinguish the off-axis one $\vec{\rho}_1$. The integrated non-rotationally symmetric NAT formulation with

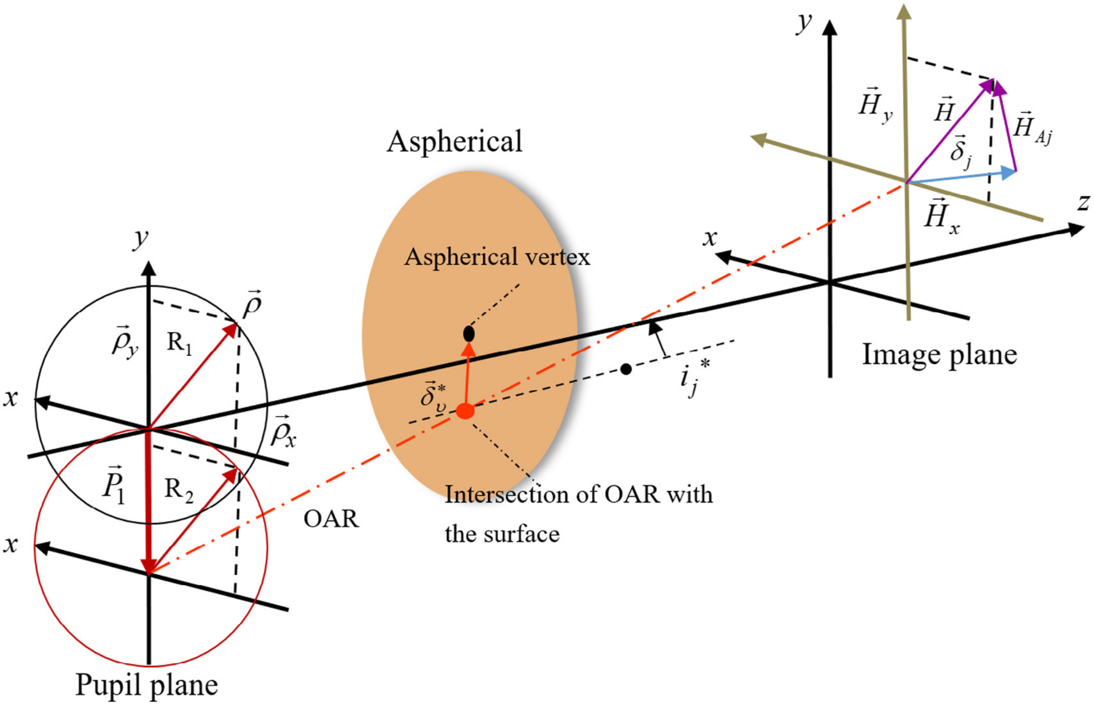

Fig. 1. Model of pupil off-axis and aberration field off-axis.

off-axis pupil and off-axis aberration field is derived as

$$
\begin{aligned}
&W_j(\vec{H},\vec{\rho}) = M^4 \sum_j \mathrm{W}_{040j}(\vec{\rho}_1\cdot\vec{\rho}_1)^2 + M^3 \\
&\times\left(4\sum_j \mathrm{W}_{040j}\vec{P} + \sum_j \mathrm{W}_{131j}(\vec{H}-\vec{\delta}_j)\right)\cdot\vec{\rho}_1(\vec{\rho}_1\cdot\vec{\rho}_1)\cdots \\
&\cdots + M^2\left(2\sum_j \mathrm{W}_{040j}\vec{P}^2 + \sum_j \mathrm{W}_{131j}\vec{P}\cdot(\vec{H}-\vec{\delta}_j)\right. \\
&\left.+\frac{1}{2}\sum_j \mathrm{W}_{222j}(\vec{H}-\vec{\delta}_j)^2\right)\cdot\vec{\rho}_1^2\cdots \\
&\cdots + M^2\left(4\sum_j \mathrm{W}_{040j}(\vec{P}\cdot\vec{P}) + \sum_j \mathrm{W}_{131j}\left[\vec{P}\cdot(\vec{H}-\vec{\delta}_j)\right]\right. \\
&\left.+\sum_j \mathrm{W}_{220mj}\left[(\vec{H}-\vec{\delta}_j)\cdot(\vec{H}-\vec{\delta}_j)\right]\right)\cdots \\
&\cdots + M\left(4\sum_j \mathrm{W}_{040j}(\vec{P}\cdot\vec{P})\vec{P} + 2\sum_j \mathrm{W}_{131j}(\vec{P}\cdot\vec{P})(\vec{H}-\vec{\delta}_j)\right. \\
&\left.+\sum_j \mathrm{W}_{131j}\vec{P}\right)\cdot\vec{\rho}_1(\vec{\rho}_1\cdot\vec{\rho}_1)\cdots \\
&\cdots + M\left(\sum_j \mathrm{W}_{222j}(\vec{H}-\vec{\delta}_j)^2\cdot\vec{P}^* + 2\sum_j \mathrm{W}_{220mj}\right. \\
&\left.\times\left[(\vec{H}-\vec{\delta}_j)\cdot(\vec{H}-\vec{\delta}_j)\right]\vec{P}\right)\cdot\vec{\rho}_1 \\
&\cdots + M\left(\sum_j \mathrm{W}_{131j}\left[(\vec{H}-\vec{\delta}_j)\cdot(\vec{H}-\vec{\delta}_j)\right](\vec{H}-\vec{\delta}_j)\right)\cdot\vec{\rho}_1
\end{aligned}
\tag{3}
$$

The superscripts of the formulas in the paper clearly express the meaning, such as *asph* regards the aspheric part and *sph* regards the spherical part. Because the field off-axis vector has no impact on the five Seidel coefficients and considering the scalarization of NAT to establish the subsequent joint aberration evaluation function, the primary aberration coefficients of NAT and the aberration coefficients of SAT are correlated as

$$
\begin{cases}
W_{040j} = W_{040j}^{(sph)} + W_{040j}^{(asph)} = \dfrac{1}{8}S_{\mathrm{I}j} \\
W_{131j} = W_{131j}^{(sph)} + W_{131j}^{(asph)} = \dfrac{1}{2}S_{\mathrm{II}j} \\
W_{222j} = W_{222j}^{(sph)} + W_{222j}^{(asph)} = \dfrac{1}{2}S_{\mathrm{III}j} \\
W_{220j} = W_{220j}^{(sph)} + W_{220j}^{(asph)} = \dfrac{1}{4}S_{\mathrm{IV}j} \\
W_{311j} = W_{311j}^{(sph)} + W_{311j}^{(asph)} = \dfrac{1}{2}S_{\mathrm{V}j}
\end{cases}
\tag{4}
$$

where $S_{\mathrm{I}j}$, $S_{\mathrm{II}j}$, $S_{\mathrm{III}j}$, $S_{\mathrm{IV}j}$, and $S_{\mathrm{V}j}$ denote the Seidel aberration coefficients of spherical, coma, astigmatism, field curvature, and distortion, respectively. And each primary wave aberration coefficient includes the spherical and aspheric contributions, respectively. The joint calculation of aberration coefficients for either two-mirror, three-mirror, or four-mirror reflective optical systems can establish the equations of structure parameters and primary aberrations. By the relationship between structural parameters and primary aberration of off-axis multiple mirrors, the aberration coefficients of different mirror numbers can correspond to the design of different types of reflective systems, respectively.

The primary wave aberration coefficients can be easily calculated by ray tracing, and the ray transfer matrix will achieve the ray tracing of ray height and angle, which is a prevalent method and will not be reviewed here. Another major central field off-axis vector has not yet been described, and the following Equation is obtained from the real ray geometry relationship (illustrated in Fig. 2) as [34]

$$
\begin{cases}
\vec{\delta}_j = \dfrac{\left[\vec{N}_j\times\left(\vec{R}_j\times\vec{S}_j\right)\right]}{\bar{u}_j+\bar{h}_j c_j} \\
\vec{\delta}_j^{(sph)} = \dfrac{{i_j}^*}{\bar{u}_j+\bar{h}_j c_j},\ \vec{\delta}_j^{(asph)} = \dfrac{{\delta_v}^*}{\bar{h}_j}
\end{cases}
\tag{5}
$$

where $\vec{N}_j$ denotes the unit normal vector of the object plane; $\vec{R}_j$ denotes the unit direction vector of the optical axis ray (OAR); $\vec{S}_j$ denotes the unit normal vector of the surface at the OAR intersection point; $\vec{\delta}_j^{(sph)}$ and $\vec{\delta}_j^{(asph)}$ denote the spherical contribution and aspheric contribution of central field off-axis vector; ${\delta_v}^*$ denotes the displacement of the center of curvature from the OAR; ${i_j}^*$ denotes the angle of incidence; c_j denotes the curvature of jth surface.

For the calculation of the deviation fitness, based on the geometric law of ray deflection (shown in Fig. 2), the angle ${i_j}^*$ of incidence can next be related to the tilt angle α_j and decenter β_j as

$$ {i_j}^* = arcsin\left(\frac{\beta_j + r_j sin(\alpha_j)}{-r_j}\right) \tag{6} $$

A relatively complete numerical calculation model of the joint aberration coefficient is established. The detailed joint aberration coefficients are derived from combined off-axis nodal aberration and Seidel aberration as follows

$$ \begin{cases} F_j^{(spherical)} = M^4 \sum\limits_j S_{\mathrm{I}j} \\ F_j^{(coma)} = M^3 \left(\left|\vec{P}_2\right| \sum\limits_j S_{\mathrm{Ij}} + \left|\vec{H} - \vec{\delta}_j\right| \sum\limits_j S_{\mathrm{II}j} \right) \\ F_j^{(astigmatism)} = M^2 \left(\left|\vec{P}_2\right| \sum\limits_j S_{\mathrm{I}j} + 2\left|\vec{P}_2 \cdot (\vec{H} - \vec{\delta}_j)\right| \sum\limits_j S_{\mathrm{II}j} \right. \\ \qquad \left. + \left|(\vec{H} - \vec{\delta}_j)^2\right| \sum\limits_j S_{\mathrm{III}j} \right) \\ F_j^{(curvature)} = M^2 \left(2\left|\vec{P}_2 \cdot \vec{P}_2\right| \sum\limits_j S_{\mathrm{I}j} + 4\left|\vec{P}_2 \cdot (\vec{H} - \vec{\delta}_j)\right| \sum\limits_j S_{\mathrm{II}j} \right. \\ \qquad \left. + \left|(\vec{H} - \vec{\delta}_j) \cdot (\vec{H} - \vec{\delta}_j)\right| (\sum\limits_j S_{\mathrm{III}j} + \sum\limits_j S_{\mathrm{IV}j}) \right) \\ F_j^{(distortion)} = M \left(\left|(\vec{P}_2 \cdot \vec{P}_2) \cdot \vec{P}_2\right| \sum\limits_j S_{\mathrm{I}j} + 2\left|(\vec{P}_2 \cdot \vec{P}_2) \cdot (\vec{H} - \vec{\delta}_j)\right| \sum\limits_j S_{\mathrm{II}j} \right. \\ \qquad + \left|\vec{P}_2^2 \cdot (\vec{H} - \vec{\delta}_j)^*\right| \sum\limits_j S_{\mathrm{II}j} \cdots \\ \cdots + \left|\vec{P}_2^* \cdot (\vec{H} - \vec{\delta}_j)^2\right| \sum\limits_j S_{\mathrm{III}j} + \left|(\vec{H} - \vec{\delta}_j) \cdot (\vec{H} - \vec{\delta}_j) \cdot \vec{P}_2\right| \\ \qquad \left. \times (\sum\limits_j S_{\mathrm{IV}j} + 2\sum\limits_j S_{\mathrm{III}j}) + \left|\left((\vec{H} - \vec{\delta}_j) \cdot (\vec{H} - \vec{\delta}_j)\right) \cdot (\vec{H} - \vec{\delta}_j)\right| \sum\limits_j S_{\mathrm{V}j} \right) \end{cases} \tag{7} $$

where $F_j^{(spherical)}$, $F_j^{(coma)}$, $F_j^{(astigmatism)}$, $F_j^{(curvature)}$, and $F_j^{(distortion)}$ are the joint aberration coefficients of spherical, coma, astigmatism, field curvature, and distortion, respectively. This section completes the mathematical modeling of the aberration coefficients of the joint aberration. It supplies the framework for the design strategy of compact volume later.

2.2. Design strategy for compact-volume system

The joint aberration can well establish the image quality evaluation function for the more complex reflective optical system. However, the volume variable easily falls into the local minimum later in optimization. Thus, it cannot obtain the optical system with excellent image quality and compact volume. Therefore, it is essential to establish an evaluation function with an initial point configuration constraint. Based on the above joint aberration model, system configuration controls are integrated, and the global SA algorithm is eventually used to obtain the initial points. The design evaluation function of off-axis reflective optical systems can be expressed as

$$ F_j = F_j^{(aberration)} + F_j^{(configuration)} \tag{8} $$

where $F_j^{(aberration)}$ denotes the joint aberration part of the evaluation function; $F_j^{(configuration)}$ represents the configuration constraints part. The joint aberration function is described by the above different aberrations related to Eq. (7) as

$$ \begin{aligned} F_j^{(aberration)} &= \mu_1 F_j^{(spherical)} + \mu_2 F_j^{(coma)} + \mu_3 F_j^{(astigmatism)} \\ &+ \mu_4 F_j^{(curvature)} + \mu_5 F_j^{(distortion)} \end{aligned} \tag{9} $$

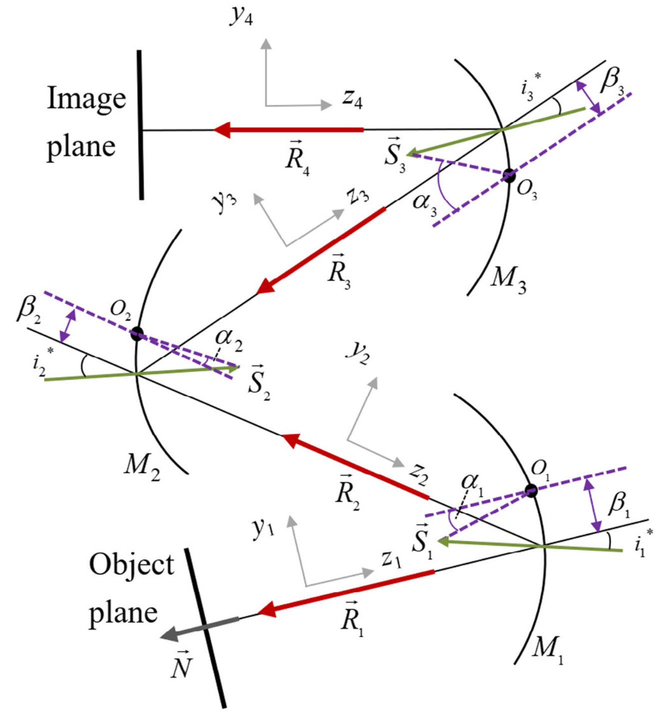

Fig. 2. Real ray-based vectors of plane-symmetric mirror system with decenter and tilt.

where μ_1, μ_2, μ_3, μ_4, and μ_5 are the weight values of aberration coefficients, including spherical, coma, astigmatism, field curvature, and distortion, respectively. Typically, off-axis reflective optical systems are more compact when the thicknesses of the adjacent mirrors are close to each other. The configuration constraints of the optical system are added to the evaluation function to obtain a compact volume as

$$ F_j^{(configuration)} = \sum_j \omega_j \left|d_1 - d_j\right| \tag{10} $$

Besides, the optimal thickness is employed as the known variable, and the interval step length is set to reduce the size. Every trait will reduce the thickness by the step length. When the evaluation function does not reach the given limit value, the volume is gradually reduced, and new thicknesses are provided as

$$ d_k = d_1 - r \cdot k \tag{11} $$

where d_k is the new thickness, d_1 is the initial value after the calculation, k is the round of computation, and r is the interval value. Therefore, the configuration-constraint function can be rewritten by

$$ F_j^{(configuration)} = \sum_1^j \sum_0^k \omega_j \left|d_1 - r \cdot k - d_j\right| \tag{12} $$

where ω_j denotes the weight value of configuration constraints. For different fields of view, the uniform sampling calculation for the full FOV is given below, and the average value of the imaging-quality evaluation function is calculated over the full FOVs as the final evaluation function value

$$ F_j^{(aberration)}(\vec{H}_x, \vec{H}_y) = \int_0^1 \int_0^1 F_j^{(aberration)} d\vec{H}_x d\vec{H}_y \tag{13} $$

where $\vec{H}_x$ and $\vec{H}_y$ denote the x and y direction FOV. The design evaluation function is obtained by combining the imaging quality and configuration evaluation functions. The function can well solve the balance issues between imaging quality and volume. The design evaluation function can be described as

$$ F_j(\vec{P}, M, d_j, r_j, k_j, \alpha_j, \beta_j) = F_j^{(aberration)} + F_j^{(configuration)} \tag{14} $$

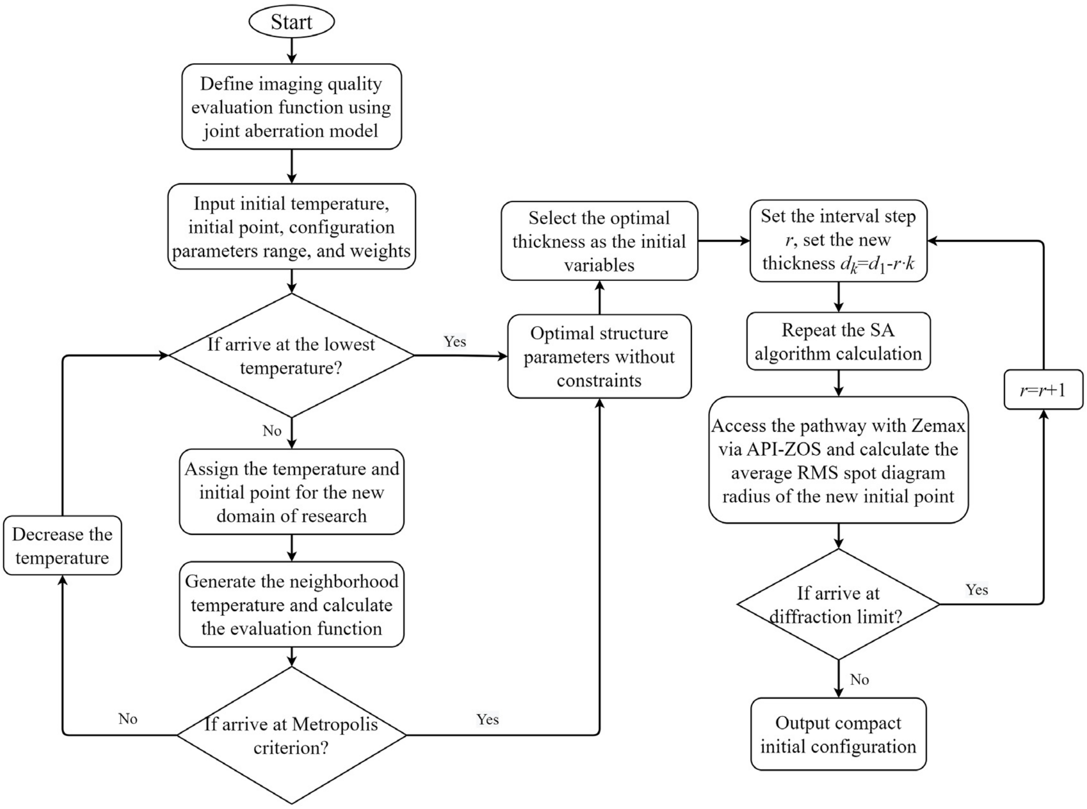

Fig. 3. The flow chart of the automatic compact-volume design process.

The operational endpoint of an evaluation function is inseparable from the criterion. This model uses API-ZOS to establish a connection between Python and Zemax, then compares the initial configuration's diffuse spot radius δ_{RMS} in the software's spot diagram to the Airy spot radius δ_{MAX} in the diffraction limit.

$$\delta_{\mathrm{RMS}} \leq \delta_{\mathrm{MAX}} \tag{15}$$

The global optimization method employed in this paper is the SA algorithm, which has been validated in earlier research [32]. The success rate of this algorithm can approach 100% in 20-trial simulations, while other types of GA, PSA, etc., can also achieve optimum outcomes. During the experiment, it is found that the criteria of different systems should be different. According to the final design results analysis, the initial criterion can employ the average RMS spot diagram radius firstly, the real criterion should be adjusted a bit, and the real criteria should be adjusted to modify different criteria for different optical systems through certain experiments (see Fig. 3).

3. Design examples

Bauer and Rolland et al. [31] explored how freeform optics allows other geometries to provide more significant benefits. However, while each of the explored geometries showed substantial improvements over their non-freeform equivalents, the "zigzag" geometry was still the strongest and most compact in terms of performance [35]. Besides, the Zernike fringe freeform presented a good performance for small-volume optimization [16]. Therefore, the "zigzag" unobscured optical systems are designed as examples, and Zernike fringe freeform surfaces are employed. The off-axis unobscured reflective optical system with "zigzag" geometry contains several types: off-axis of FOV, off-axis of the pupil, and off-axis system with decenter and tilt.

Table 1
Specifications of the off-axis three-mirror reflective optical system.

Parameter	Specification
Focal length	600 mm
F-number	6
Working spectrum	380~760 nm
Full field of view	16° × 1°
MTF (150 lp/mm)	≥0.3

3.1. Small-volume off-axis three-mirror system design with a large FOV

As the FOVs expand, the aberrations become considerably harder to correct. Therefore, the designs of an off-axis three-mirror reflective system with large FOVs are taken as an example to demonstrate the feasibility and convenience of automatic optimization modeling. The optical system specification is presented in Table 1. The focal length of this off-axis three-mirror reflective optical system is 600 mm, F-number is 6, and FOV is 16° × 1°, which can meet the requirements of the space optical camera. The initial points can be directly designed by this method. As mentioned, the final off-axis three-mirror reflective optical system is original to the initial configurations with conicoid surfaces.

The off-axis-based initial configuration design method, i.e., the conventional design method, uses the automatic global solution method of joint aberration as a comparison experiment for design. After the calculation by the SA algorithm, the initial optimal configuration parameters can be obtained without the volume constraints. The initial configuration and the optimization results are shown in Fig. 4. The final optimized layout is comparable to the initial design, the spot diagram radii are all in the airy disk, and the imaging quality is nearly the diffraction limit. The modulation transfer function (MTF) shows it is larger than 0.3 at 150 lp/mm. The optical system is designed from three simple Conic surfaces with an integrated primary–tertiary mirror. The primary and tertiary mirrors are Zernike fringe freeform surfaces with the first 25 plane-symmetry coefficients (13 terms in total). The strategy has made it possible to automate the off-axis reflective optical

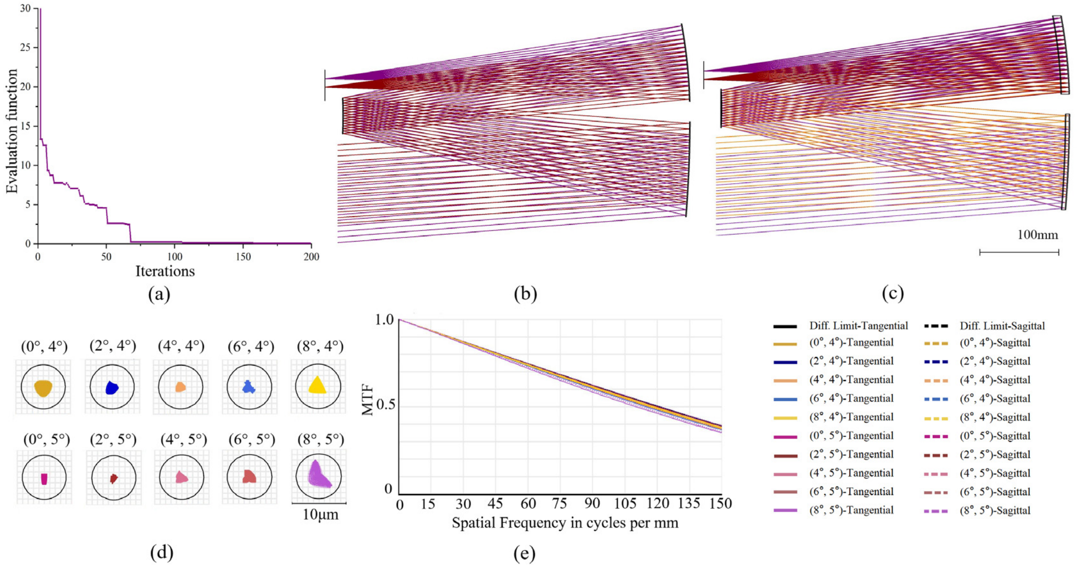

Fig. 4. The off-axis three-mirror reflective optical system with a 16° × 1° FOV. (a) The iteration process of the imaging performance evaluation function, (b) The initial configuration layout, (c) The optimized reflective optical system layout based on the initial configuration, (d) The spot diagram of the optimized reflective optical system, (e) The modulation transfer function of the optimized reflective optical system.

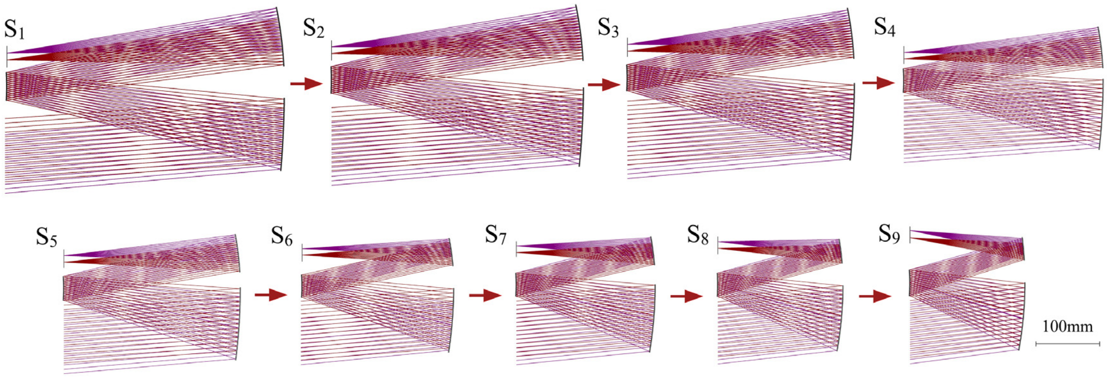

Fig. 5. The optical system layouts of compact-volume starting point with a 16° × 1° FOV.

system design, substantially lowering the time necessary to locate the initial structure from coaxial optical systems or even patent libraries and reducing the complexity of off-axis reflective optical systems. But it exhibits a relatively large volume, different from the design concept of lightweight miniaturization. This automatic initial structure design method is developed based on the traditional design method and utilizes an alternative global algorithm for calculation.

In contrast to the above approach, the design method combining the imaging-performance evaluation function and volume-constraint evaluation function is more effective, fast, and simple to achieve optical systems with high image quality and small volume. Based on the model of the theoretical part, the range of parameters of the initial structure parameters is given first, including the off-axis vector of the pupil, the radii of curvature, the mirror distances, the conic values of the aspheric surfaces, etc. Here, depending on the design experience, a smaller range can be given. In the absence of experience, however, the capacity of the solution space can be increased, and the same excellent starting point can be attained, despite a longer calculation time. In the absence of special requirements, the weight values of the evaluation functions can all be set to 1. For a specific design result with a large aberration, it is a promising approach to increase the weight value of its aberration coefficient.

The initial thickness parameters are about 440 mm, and 440 mm is taken as the initial thickness value. The model employs a reduced step interval of 40 mm to enhance computational performance, and the results are reported after each round (seen in Fig. 5). Initial points S_1~S_6 are computed using 40 mm interval increments, resulting in spot diagram radii which are all less than the Airy spot radius. The initial configuration parameters are about 440 mm, and 440 mm is taken as the initial thickness value. In the subsequent calculation, the thickness reduction step value was replaced by 20 mm, and the criterion of the spot diagram radius was increased to 10 μm to search for the optimal initial configuration. Eventually, the simulation results of S_6~S_9 were obtained.

The volumes of the 9 rounds S_1~S_9 are 51.68L, 42.03L, 35.35L, 24.09L, 19.30L, 16.71L, 14.39L, 11.14L, and 9.31L, respectively, from largest to smallest. This approach compresses the volume of such systems to 22.7% of the conventional method S_1, achieving a large extent of compression of the initial configuration volume. Among them, the specific structure parameters of all rounds in the volume compression process are shown in Table 2. The mirror distance regularly decreases downward, leading to a gradual decrease in volume.

Based on these simple Conic surfaces, the freedom of the surface type is increased to obtain better imaging results. A simple optimization is performed directly according to the initial point to get a reflective optical system design with seemingly good quality. Meanwhile, the optimization, image quality evaluation, and result analysis are carried out for three different surface types. $S^{(CCC)}$ denotes the design with three

Table 2
Specifications of off-axis reflective three-mirror initial configuration.

No	r_1 (mm)	r_2 (mm)	r_3 (mm)	d_1 (mm)	d_2 (mm)	d_3 (mm)	k_1	k_2	k_3
1	−1565.30	−449.17	−627.23	−440.00	440.00	−440.00	−1.30	0.81	0.20
2	−1387.85	−413.48	−586.23	−400.00	400.00	−400.00	−1.32	0.46	0.20
3	−1220.94	−379.01	−547.04	−360.00	360.00	−360.00	−1.33	0.07	0.19
4	−1064.06	−346.42	−510.87	−320.00	320.00	−320.00	−1.33	−0.36	0.16
5	−915.98	−315.68	−479.77	−280.00	280.00	−280.00	−1.89	−0.89	−0.17
6	−780.28	−293.13	−462.46	−240.00	240.00	−240.00	−1.34	−1.60	−0.31
7	−717.48	−287.06	−465.52	−220.00	220.00	−220.00	−1.35	−2.11	−0.90
8	−660.50	−290.20	−490.01	−200.00	200.00	−200.00	−1.38	−2.90	−2.65
9	−601.32	−292.10	−546.16	−180.00	180.00	−180.00	−1.41	−3.79	−10.00

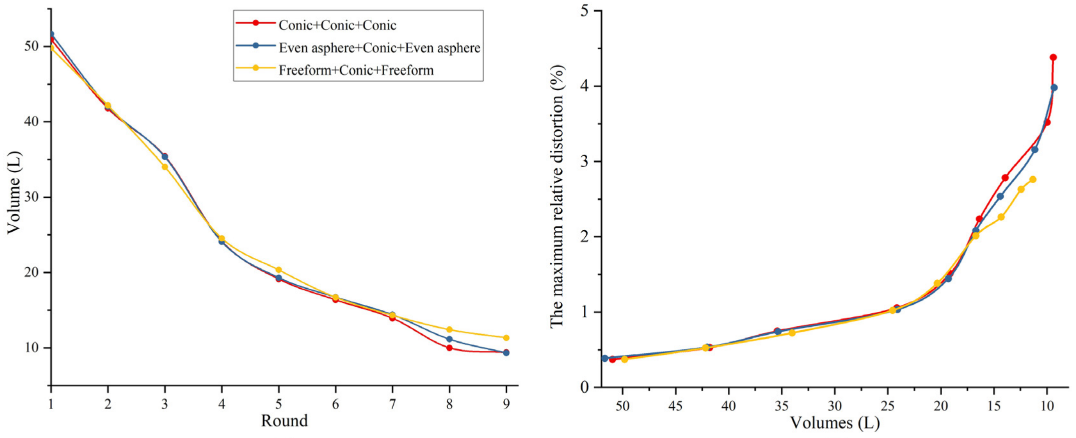

(a) (b)

Fig. 6. The volumes and distortion comparison of the calculation process. (a) The volume variation of different surface types, (b) The maximum relative distortion comparison of three various surfaces.

conic surfaces, $S^{(\mathrm{ECE})}$ means the design with two even aspheric surfaces (primary and tertiary mirrors) and a conic surface (secondary mirror), $S^{(\mathrm{FCF})}$ represents the design with two Zernike Fringe freeform surfaces (primary and tertiary mirrors) and a conic surface (secondary mirror). To facilitate the subsequent description of the imaging quality and the design analysis, the systems of the three surface combinations are named $S^{(\mathrm{CCC})}$, $S^{(\mathrm{ECE})}$, and $S^{(\mathrm{FCF})}$, respectively. As optimization variables, the even aspheric surfaces use the higher order terms of 4, 6, and 8, whereas the Zernike freeform surfaces use the first 37 plane-symmetry coefficients (20 terms in total). After introducing the optimization of various mirror types, the deviation of the system volume is evaluated for the two types of surface shapes relative to the volume of the initial structure, revealing that volume deviation (illustrated in Fig. 6a) for the three types is low, with an error rate of 3.94% compared to the volume of the initial configuration. The maximum relative distortion values (illustrated in Fig. 6b) of systems S_1~S$_9$ are 0.37%, 0.53%, 0.75%, 1.06%, 1.51%, 2.24%, 2.78%, 3.52%, and 4.38%, respectively. Although the distortion value is a bit large, it is relatively simple to correct in the subsequent optimization process by optical design software or imaging process methods. When the volume is larger than 18L, $S^{(\mathrm{CCC})}$, $S^{(\mathrm{ECE})}$, and $S^{(\mathrm{FCF})}$ present similar aberration performance, indicating that the effect of complex surface types on aberrations is not apparent when simple optimization is performed. In comparison, for a smaller volume, the design of three surface type combinations demonstrates better correction from the more complex surface types in controlling aberrations.

In general, the average root means square (RMS) radius of the spot diagram and the average RMS wavefront error (WFE) (shown in Fig. 7) can be evaluated more comprehensively for $S^{(\mathrm{CCC})}$, $S^{(\mathrm{ECE})}$ and $S^{(\mathrm{FCF})}$. The average RMS spot diagram radius curve can describe that when the larger volumes are kept higher than around 21L, the imaging quality of $S^{(\mathrm{CCC})}$, $S^{(\mathrm{ECE}),}$ and $S^{(\mathrm{FCF})}$ can arrive at nearly the diffraction limit. For smaller volumes, only $S^{(\mathrm{ECE})}$ and $S^{(\mathrm{FCF})}$ can achieve image quality close to the diffraction limit, while the imaging quality of $S^{(\mathrm{CCC})}$ deteriorates rapidly. Such analysis assists in the optical design process by selecting a design that fulfills the design requirements and more straightforward surfaces. If the conditions for imaging performance are low, you may choose a more easily achievable surface type, such as $S^{(\mathrm{CCC})}$ and $S^{(\mathrm{ECE})}$. Its analyses enable a good feasibility estimation of the volume of the optical system. The freeform mirrors are employed to gain the final reflective optical system with an excellent and small volume. The freeform includes 20 available plane-symmetry Zernike fringe coefficients of a maximum of 37 terms. The optimized optical system is original from the initial point S_9, and the layout (seen in Fig. 8a) is comparable to the initial configuration. The imaging performance is excellent by the spot diagram (illustrated in Fig. 8b) and MTF curves (shown in Fig. 8c). The spot diagram radii of all FOVs are within the Airy spot disk, and MTF values are greater than 0.3 at 150lp/mm, which indicates excellent imaging quality.

This section clarifies the global solution design method based on the integrated evaluation function, which automates the volume compression of the initial point and saves the designer's design time. The volume compression effect is quite evident, and the design of different types of faces demonstrates the feasibility and effectiveness of this design method. The method serves as a practical reference for the design of small-volume space optical cameras and telescopes. This method is also applicable for more complex off-axis three-mirror reflective optical systems with small F-number, decenter, and tilt, as elaborated by the second design example below.

3.2. Small-volume three-mirror imager design with tilt and decenter

The second part of the design example revolves around volume compression of infrared small F-number off-axis three-mirror reflective optical systems. The design specifications of the system are listed in Table 3, with a focal length of 110 mm, an F-number of 2, an FOV of 6° × 6°, and a waveband covering the infrared band of 8~12 μm.

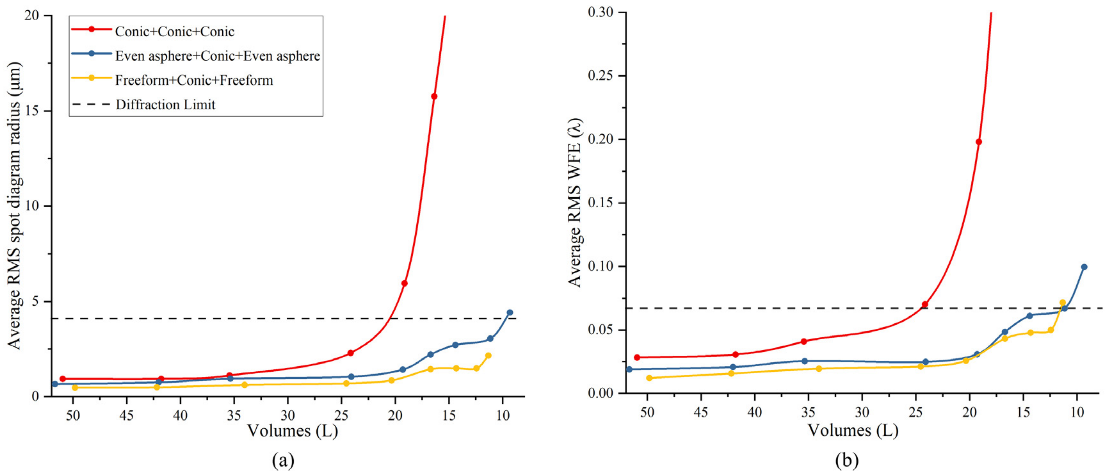

Fig. 7. The wavefront error and spot diagram radius comparison of aspherical, even aspherical, and freeform systems. (a) Average RMS WFE curve by the volumes ($\lambda = 550$ nm), (b) Average RMS spot diagram radius by volumes.

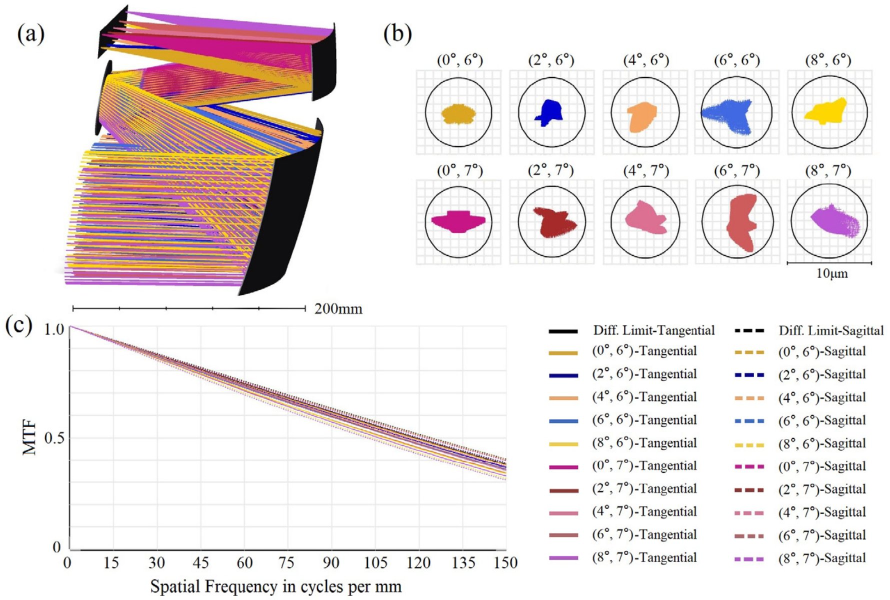

Fig. 8. The final optimization of the compact-volume reflective optical system. (a) The Zernike freeform reflective optical system layout, (b) Spot diagram, (c) MTF curves.

Table 3
Specifications of the off-axis three-mirror reflective optical system.

Parameter	Specification
Focal length	110 mm
F-number	2
Working spectrum	8~12 μm
Full field of view	6° × 6°

The initial points S_1~S_7 are calculated by the interval step value of 10 mm (illustrated in Fig. 9), and the spot diagram radii are all lower than Airy spot radius (the criterion value). From the largest to smallest volume, the seven rounds S_1~S_7 are 1.60L, 1.44L, 1.13L, 0.99L, 0.78L, 0.61L, and 0.45L, respectively. This approach compresses the volume of such systems to 28.3% of the conventional method, achieving a large extent of compression of the initial configuration volume. The details of initial configurations are presented in Table 4, which is obviously the same interval to reduce the thickness step by step. Until the imaging quality of RMS spot diagram radius arrives at the diffraction limit, the iteration will be stopped. The design S_7 is the final design after the iteration calculation. The criterion value can be increased to get a wider range of initial configurations if the surface complexity improves.

Although the initial design has a bad imaging performance, the off-axis reflective optical system can still own good imaging performance by adding surface complexity. Three-type surfaces are loaded in the initial conicoid surfaces based on good starting points. The $S^{(CCC)}$ means the optical system with three conic surfaces, $S^{(ECE)}$ denotes the system with two even aspherical surfaces (primary and tertiary mirror) and a Conic surface (secondary mirror), the even aspherical surfaces including 4th, 6th, 8th, and 10th higher-term coefficients. $S^{(FFF)}$ denotes the system with three freeform, which have the 20 plane-symmetry coefficients of 37 Zernike fringe freeform coefficients. After optimizing various mirror types, the system volume is evaluated for the two types of surface shapes relative to the volume of the starting structure, indicating that volume deviation (shown in Fig. 10a) for the three types is low, with an error rate of 4.26%. The maximum relative distortion (illustrated in Fig. 10b) of initial systems S_1~S_7 are 2.34%, 2.24%, 2.82%, 3.18%, 3.86%, 4.38, and 5.03%, respectively. In this case, the maximum relative distortion values of the systems with freeform surfaces are larger than others. The potential reason is

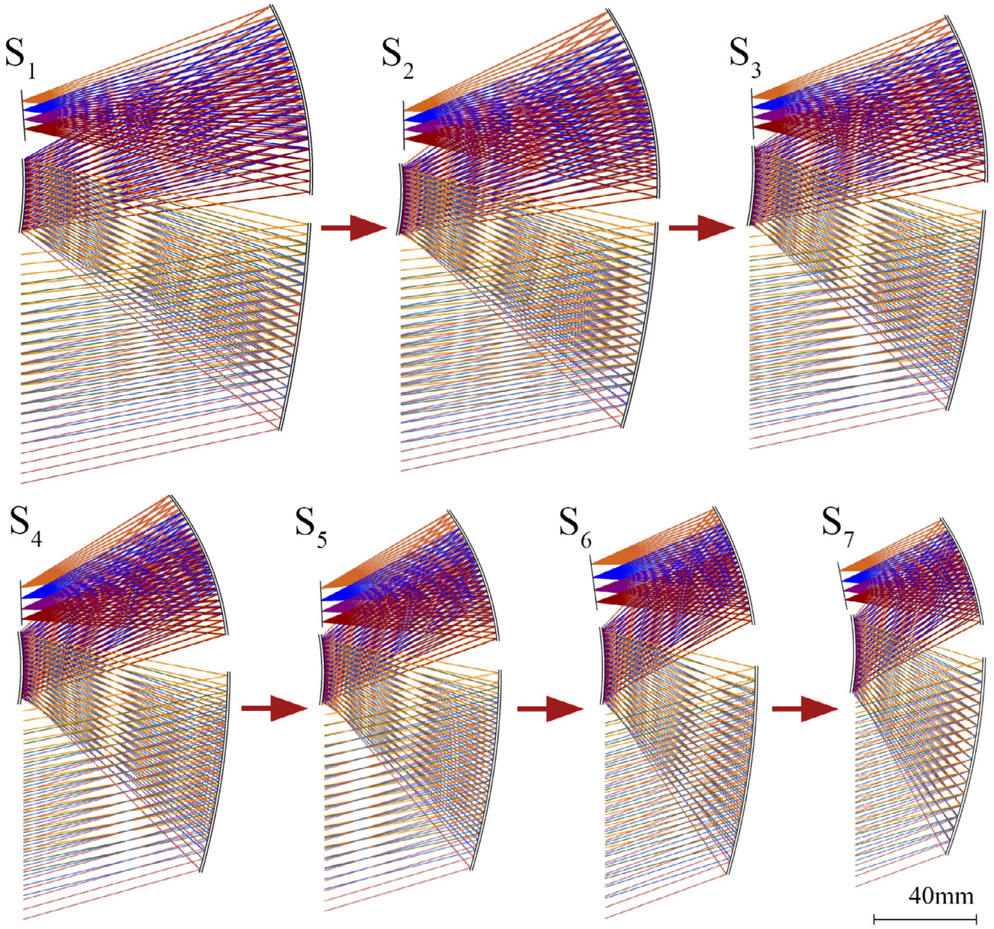

Fig. 9. The optical system layouts of compact-volume starting points with F-number 2.

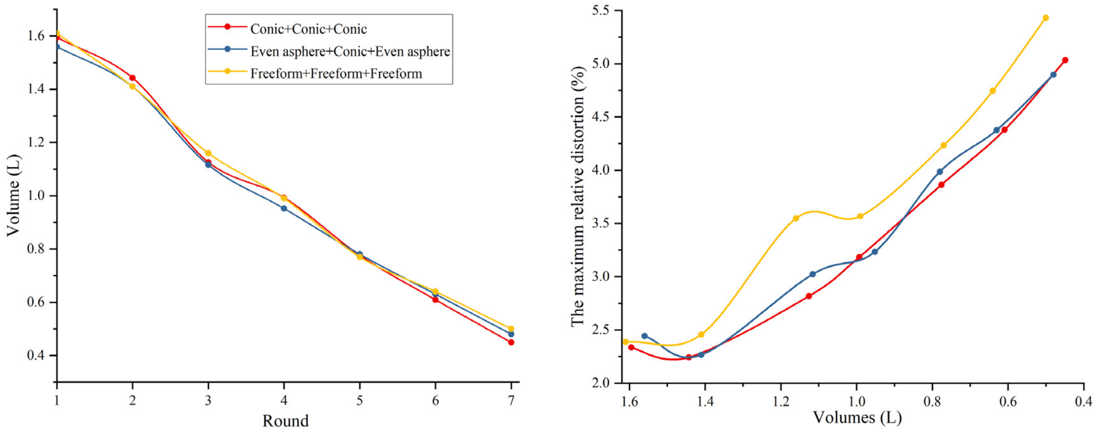

(a)

(b)

Fig. 10. The volumes and distortion comparison of the calculation process. (a) The volume variation of different surface types, (b) The maximum relative distortion comparison of three various surfaces.

Table 4
Specifications of off-axis reflective three-mirror initial configuration.

No	r_1 (mm)	r_2 (mm)	r_3 (mm)	d_1 (mm)	d_2 (mm)	d_3 (mm)	k_1	k_2	k_3
1	−475.18	−127.39	−150.45	−110.00	110.00	−110.00	−1.63	2.54	0.24
2	−417.90	−120.13	−140.30	−100.00	100.00	−100.00	−1.63	2.16	0.25
3	−373.39	−118.27	−131.93	−90.00	90.00	−90.00	−3.11	1.23	0.29
4	−297.22	−91.42	−117.37	−80.00	80.00	−80.00	−1.47	0.66	0.23
5	−252.23	−82.94	−107.81	−70.00	70.00	−70.00	−1.49	0.11	0.20
6	−226.16	−90.51	−105.67	−60.00	60.00	−60.00	−1.72	−0.65	0.03
7	−170.74	−64.88	−92.06	−50.00	50.00	−50.00	−1.25	−0.43	−0.05

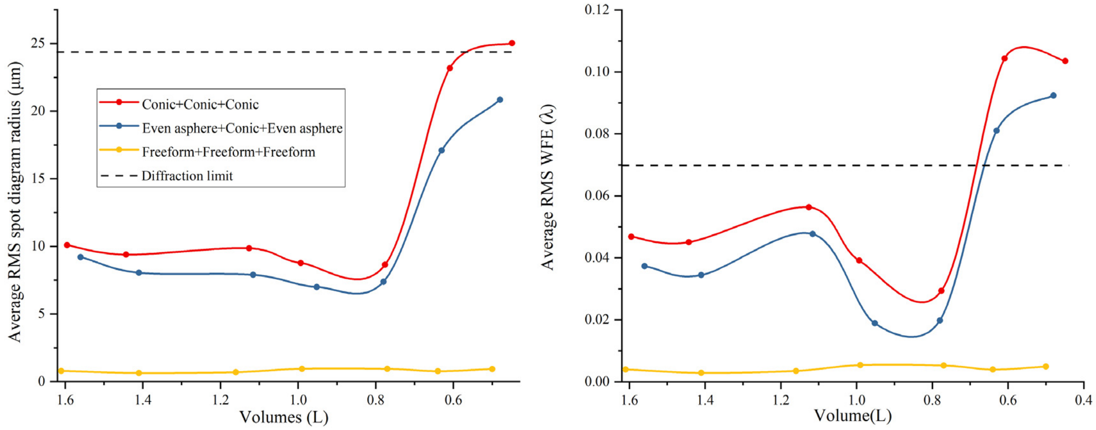

(a) (b)

Fig. 11. The wavefront error and spot diagram radius comparison of aspherical, even aspherical, and freeform systems. (a) Average RMS WFE curve by the volumes ($\lambda = 10$ μm), (b) Average RMS spot diagram radius by volumes.

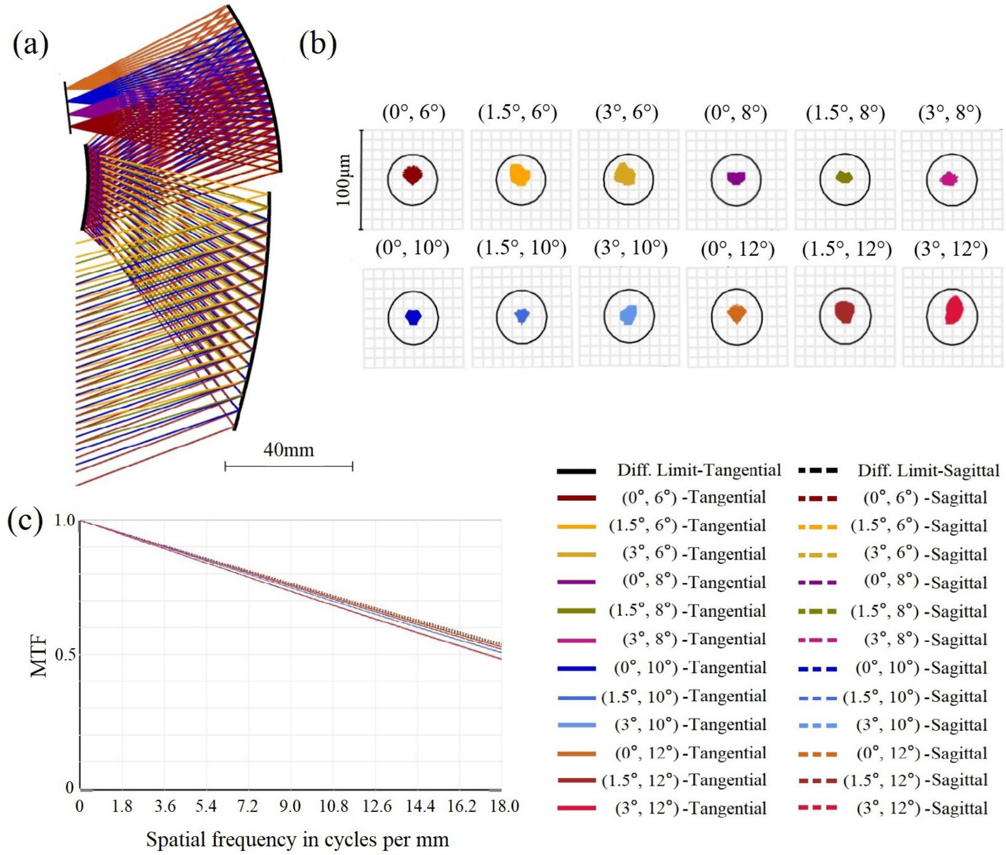

Fig. 12. The final optimization of the small-volume optical system with F-number 2. (a) The layout of the Zernike freeform reflective optical system, (b) Spot diagram, (c) MTF curves.

that the aberration is balanced by sacrificing distortion in the optimization process. The distortion performance is subsequently controlled by adding operands to the merit function in Zemax, and the aberrations are corrected effectively by the imaging process methods.

Next, the imaging quality of these systems is analyzed. When the volumes are smaller than around 0.6L, the average RMS spot diagram radii (seen in Fig. 11a) are all lower than the line of the diffraction limit. When the volumes are lower around 0.7L, the average RMS WFE of $S^{(\mathrm{CCC})}$, $S^{(\mathrm{ECE})}$, and $S^{(\mathrm{FFF})}$ are in the same position to be lower than 0.07λ ($\lambda = 10$ μm). All cases show us good imaging performance with a compact volume. Moreover, it is easy to find that the imaging quality of $S^{(\mathrm{FFF})}$ has been stable so that the criterion value can be further increased. The Airy spot radius in the diffraction limit as a criterion is worth discussing, and more experiments are needed for subsequent verification.

The experiments mentioned above also illustrate the effectiveness of this design method on volume compression. Finally, a small-volume freeform off-axis three-mirror unobscured optical system (shown in

Fig. 12a) is designed based on this initial points calculation method. The compact optical system is original from the initial point S_7, which looks like the initial configuration. The imaging performance is excellent by the spot diagram (illustrated in Fig. 12b) and MTF curves (shown in Fig. 12c), the spot diagram radii of full FOVs are within the Airy spot disk, which indicates the excellent imaging quality, as well as MTF curves. The average RMS WFE is about 0.004λ ($\lambda = 10$ μm). Since the average wavefront difference is well above the diffraction limit, the design can have space for volume compression. However, we stop at this point considering distortion and other issues. The choice of the precise structure parameters range, the criterion values applicable to different types of systems, etc., need to be investigated with much more effort. The excellent performance results on volume compression prove the reference value of the method. The design approach applies equally to reflective optical designs with large FOVs for two and four mirrors.

4. Conclusion

Traditional off-axis reflective optical system designs frequently focus on imaging quality, while the volume is reduced later in the optimization process. If the starting volume is too large, the designer spends much time finding a design result that meets the design requirements. At the same time, the complexity of the surface shape cannot be simplified during the volume reduction optimization process. Therefore, an excellent initial configuration is crucial. Firstly, this paper proposes an automated design for the starting point of a small-volume reflective optical system. The method offers an innovative global optimization of the joint aberration and finds an initial optical system with excellent imaging quality and compact volume by iteration reduction of a global SA algorithm. The second point is that the method presented in this paper uses a simple conicoid surface type as the starting point, which is more expandable when combined with conventional optical design software. It also facilitates the research and analysis of aberration for the intermediate process, making the design more straightforward and efficient. Finally, by showing design examples and extending to the discussion of different face shapes, it helps designers to estimate the optimal volume according to the design requirements at the early stage of design and guides the selection of surfaces. So far, the design method in this study focuses on planar symmetric off-axis reflective optical systems, and we will continue to develop the design method for more complex non-planar symmetric systems in future research.

Declaration of competing interest

The authors declare the following financial interests/personal relationships which may be considered as potential competing interests: Zheng Qu reports financial support was provided by National Key Research and Development Program of China.

Data availability

No data was used for the research described in the article.

Acknowledgments

The authors acknowledge the technical support provided by the Optical Design Laboratory of Chang Guang Satellite Technology Co., Ltd.

Funding

This work was supported by National Key Research and Development Program of China [Grant number 2019YFE0127000].

References

[1] D. Korsch, Anastigmatic three-mirror telescope, Appl. Opt. 16 (1977) 2074–2077.
[2] X. Liu, T. Gong, G. Jin, J. Zhu, Design method for assembly-insensitive freeform reflective optical systems, Opt. Express 26 (2018) 27798–27811.
[3] Q. Meng, H. Wang, W. Liang, Z. Yan, B. Wang, Design of off-axis three-mirror systems with ultrawide field of view based on an expansion process of surface freeform and field of view, Appl. Opt. 58 (2019) 609–615.
[4] J.M. Rodgers, Unobscured mirror designs, in: Int. Opt. Des. Conf. 2002, SPIE, 2002, pp. 33–60.
[5] R. Gilmozzi, J. Spyromilio, The European Extremely Large Telescope (E-ELT), Messenger 127 (2007) 11–15.
[6] M. Johns, P. McCarthy, K. Raybould, A. Bouchez, A. Farahani, J. Filgueira, G. Jacoby, S. Shectman, M. Sheehan, Giant magellan telescope - Overview, Proc. SPIE - Int. Soc. Opt. Eng (2012).
[7] G. Sanders, The thirty meter telescope (TMT): An international observatory, J. Astrophys. Astron. 34 (2013) 81–86.
[8] V. Batshev, S. Bodrov, A compact three-mirror astronomical objective, Instrum. Exp. Tech. 59 (2016) 557–561.
[9] N. Ersumo, C. Yalcin, N. Antipa, N. Pegard, L. Waller, D. López, R. Muller, A micromirror array with annular partitioning for high-speed random-access axial focusing, Light Sci. Appl. 9 (2020) 183.
[10] Y. Liu, Y. Li, Z. Cao, Design method of off-axis extreme ultraviolet lithographic objective system with a direct tilt process, Opt. Eng. 54 (2015) 75–102.
[11] C. Liu, C. Straif, T. Flügel-Paul, U. Zeitner, H. Gross, Comparison of hyperspectral imaging spectrometer designs and the improvement of system performance with freeform surfaces, Appl. Opt. 56 (2017) 68–94.
[12] J.P. Rolland, M.A. Davies, T.J. Suleski, C. Evans, A. Bauer, J.C. Lambropoulos, K. Falaggis, Freeform optics for imaging, Optica 8 (2021) 161–176.
[13] P. Robb, Three-mirror telescopes: design and optimization, Appl. Opt. 17 (1978) 2677–2685.
[14] L.G. Cook, Three-mirror anastigmat used off-axis in aperture and field, in: Proc. SPIE, Space Optics, Vol. 183, 1979, pp. 207–211.
[15] J. Reimers, A. Bauer, K. Thompson, J. Rolland, Freeform spectrometer enabling increased compactness, Light Sci. Appl. 6 (2017) e17026.
[16] E.M. Schiesser, A. Bauer, J.P. Rolland, Effect of freeform surfaces on the volume and performance of unobscured three mirror imagers in comparison with off-axis rotationally symmetric polynomials, Opt. Express 27 (2019) 21750–21765.
[17] X. Liu, J. Zhu, Automatic design method of starting points of freeform off-axis reflective imaging systems of small volume, Opt. Express 30 (2022) 7954–7967.
[18] L. Chen, Z. Gao, N. Xu, X. Cao, J. Zhang, L. Wang, J. Ye, Q. Yuan, Construction of freeform mirrors for an off-axis telecentric scanning system through multiple surfaces expansion and mixing, Results Phys. 19 (2020) 103354.
[19] Y. Zhang, xu Wang, Z. Su, H. Pan, X. Chen, W. Zhang, Design freeform optical surface in off-axis reflective imaging system by a double seed curve extension algorithm, Appl. Opt. 60 (2021) 9193–9205.
[20] L. Jun, W. Huang, F. Hongjie, A novel method for finding the initial structure parameters of optical systems via a genetic algorithm, Opt. Commun. 361 (2016) 28–35.
[21] C. Cao, S. Liao, Z. Liao, Y. Bai, Z. Fan, Initial configuration design method for off-axis reflective optical systems using nodal aberration theory and genetic algorithm, Opt. Eng. 58 (2019) 105101.
[22] X. Yu, H. Wang, Y. Yao, S. Tan, Y. Xu, Y. Ding, Automatic design of a mid-wavelength infrared dual-conjugate zoom system based on particle swarm optimization, Opt. Express 29 (2021) 14868–14882.
[23] W. Chen, T. Yang, D. Cheng, Y. Wang, Generating starting points for designing freeform imaging optical systems based on deep learning, Opt. Express 29 (2021) 27845–27870.
[24] C. Fan, B. Yang, Y. Liu, Q. Zhao, B. Qian, S. Chen, Using deep learning to automatically generate design starting points for free-form imaging optical systems, Appl. Opt. 61 (2022) 6241–6248.
[25] J. Zhu, X. Wu, T. Yang, G. Jin, Generating optical freeform surfaces considering both coordinates and normals of discrete data points, J. Opt. Soc. Amer. A 31 (2014) 2401–2408.
[26] D. Cheng, Y. Wang, H. Hua, Free form optical system design with differential equations, Proc. SPIE - Int. Soc. Opt. Eng. 7849 (2010).
[27] Y. Nie, H. Thienpont, F. Duerr, Multi-fields direct design approach in 3D: Calculating a two-surface free form lens with an entrance pupil for line imaging systems, Opt. Express 23 (2015) 34042–34054.
[28] T. Yang, J. Zhu, W. Hou, G. Jin, Design method of freeform off-axis reflective imaging systems with a direct construction process, Opt. Express 22 (2014) 9193–9205.
[29] T. Yang, J. Zhu, X. Wu, G. Jin, Direct design of freeform surfaces and freeform imaging systems with a point-by-point three-dimensional construction-iteration method, Opt. Express 23 (2015) 10233–10246.

[30] Y. Zhong, H. Gross, Initial system design method for non-rotationally symmetric systems based on Gaussian brackets and nodal aberration theory, Opt. Express 25 (2017) 10016–10030.

[31] A. Bauer, E.M. Schiesser, J.P. Rolland, Starting geometry creation and design method for freeform optics, Nature Commun. 9 (2018) 1–11.

[32] Z. Qu, X. Zhong, K. Zhang, L. Li, Y. Wang, Automatic initial configuration in off-axis reflective optical system design using combined nodal and seidel aberration, Appl. Opt. 61 (2022) 3630–3640.

[33] K.P. Thompson, Description of the third-order optical aberrations of near-circular pupil optical systems without symmetry, J. Opt. Soc. Amer. A 22 (2005) 1389–1401.

[34] K.P. Thompson, T. Schmid, O. Cakmakci, J.P. Rolland, Real-ray-based method for locating individual surface aberration field centers in imaging optical systems without rotational symmetry, J. Opt. Soc. Amer. A 26 (2009) 1503–1517.

[35] A. Bauer, J.P. Rolland, Roadmap for the unobscured three-mirror freeform design space, Opt. Express 29 (2021) 26736–26744.